COMMUNICATION

Check for updates

A graphene quantum dot decorated SrRuO₃ mesoporous film as an efficient counter electrode for high-performance dye-sensitized solar cells†

Tao Liu,[a] Kun Yu,[a] Lina Gao,[a] Hui Chen,[a] Ning Wang,*[b] Luhan Hao,[c] Tingxi Li,*[d] Hongcai He[a] and Zhanhu Guo [ID] *[c]

Hydrothermally synthesized electrically conductive perovskite strontium ruthenate (SrRuO₃) nanoparticles were added into a binder solution and then cast onto fluorine doped tin oxide (FTO) glass to form a mesoporous SrRuO₃ counter electrode (CE) for dye-sensitized solar cells (DSSCs). The high porosity and large specific surface area of the SrRuO₃ CE allows easier and faster diffusion of electrolyte into the pores and involves more triiodide (I_3^-) in the redox reaction, thereby resulting in a higher power conversion efficiency (PCE, 7.16%) than that of our published research on sputtered SrRuO₃ film CEs (6.48%). Furthermore, graphene quantum dots (GQDs) endowed with excellent intrinsic catalytic activity and high conductivity were decorated onto the SrRuO₃ CE by a dipping technique to form a SRO–GQD hybrid. The synergistic effect of SrRuO₃ and GQDs contributes to more active catalytic sites as well as faster ion diffusion and electron transfer than a pristine SrRuO₃ CE, thereby resulting in increased electrocatalytic ability towards I_3^- reduction. As a result, our fabricated DSSCs based on the optimized SRO–GQD CE achieve an impressive PCE of 8.05%, much higher than that of the reference device assembled with a conventional platinum (Pt) CE (7.44%). The SRO–GQD CE also exhibits an excellent long-term electrochemical stability in I_3^-/I^- electrolyte. Overall, the SRO–GQD hybrid can be considered as a highly efficient Pt-free CE for practical applications of DSSCs.

1. Introduction

Dye-sensitized solar cells (DSSCs), a promising alternative to conventional photovoltaic devices, are attracting widespread interest due to their low cost, easy fabrication, and high power conversion efficiency (PCE).[1] As one of the important components, a counter electrode (CE) collects electrons from external circuits, and catalyzes the reduction of triiodide (I_3^-) to iodide (I^-), which involves a critical dye regeneration reaction.[2] Among all materials that have been explored, platinum (Pt) remains the most widespread choice for CEs, owing to its high electrical conductivity and excellent electro-catalytic activity, which are both essential properties for a high-efficiency CE. However, Pt can be easily decomposed into PtI_4 in the electrolyte containing an I_3^-/I^- redox couple, which is detrimental to the device's long-term stability.[2a,3] Furthermore, as a noble metal, its scarcity and high cost remain an obstacle for large-scale production and commercial application of DSSCs. Hence, it is imperative to develop promising Pt-free alternatives with low cost, corrosion resistance, high conductivity and outstanding catalytic activity. The most promising candidates for this substitution include various types carbon-based materials,[4] conductive polymers,[5] and inorganic compounds.[6]

Electrically conductive perovskites (ABO₃, *e.g.* SrRuO₃) (A: alkaline earth or lanthanide; B: transition metal element) have been widely used to replace conventional Pt as anode catalysts for hydrogen evolution reactions[7] as well as electro-oxidation in direct alcohol fuel cells.[8] Recently, our research group reported for the first time a sputtered SrRuO₃ film as a Pt-free CE in DSSCs, which provides a new perspective that the electro-catalytic activity towards I_3^- reduction is closely related to the lattice mismatch between the sputtered SrRuO₃ film and the substrate *via* epitaxial strain. Nevertheless, the relatively high charge-transfer resistance leads to low fill factor (FF) values (<0.6), which consequently results in a poor PCE value (6.48%).[9]

Owing to their good catalytic activities toward I_3^- reduction, excellent resistances to iodine, high electrical conductivities, earth-abundances, and low costs, great progress has been made in carbon-based CE materials. In particular, graphene is a promising two-dimensional sheet of a single atomic layer of carbon with sp²-hybridized orbitals, exhibiting excellent carrier mobility and conductivity, chemical inertness and electro-catalytic activity.[10] As a new type of graphene nanostructure,

[a]*State Key Laboratory of Electronic Thin Film and Integrated Devices, University of Electronic Science and Technology of China, Chengdu 610054, P. R. China*

[b]*State Key Laboratory of Marine Resource Utilization in South China Sea, Hainan University, Haikou 570228, P. R. China. E-mail: wangninguestc@gmail.com*

[c]*Integrated Hybrid Lab (ICL), Department of Chemical & Biomolecular Engineering, University of Tennessee, Knoxville, Tennessee, 37966, USA. E-mail: zguo10@utk.edu*

[d]*College of Materials Science and Engineering, Shandong University of Science and Technology, Qingdao 266590, China. E-mail: litx@sdust.edu.cn*

† Electronic supplementary information (ESI) available. See DOI: 10.1039/c7ta05123a

graphene quantum dots (GQDs) exhibit good crystallinity and possess the same lattice structure as graphene.[4a] Owing to quantum confinement and edge effects, GQDs have generated great interest in both the fundamental science and potential applications in photovoltaic devices, fuel cells, and light-emitting diodes.[11] In particular, according to recent research, the addition of GQDs could enhance the catalytic activity of CEs, such as polyaniline/GQD nanocomposite CEs,[12] GQDs doped polypyrrole CEs,[13] and GQD-decorated mesoporous carbon aerogel composite CEs.[4a]

In the present work, a GQD decorated mesoporous $SrRuO_3$ film (SRO–GQD) CE was successfully prepared by a dipping technique, and the electrocatalytic abilities have been evaluated by cyclic voltammetry (CV), electrochemical impedance spectroscopy (EIS) and Tafel polarization. The mesoporous $SrRuO_3$ film is prepared via a spin-coating method, in which $SrRuO_3$ nanoparticles were added into a binder to form a paste, and then cast onto the fluorine doped tin oxide (FTO) substrate, followed by annealing at 450 °C for 30 min. It should be noted that there are few reports on the preparation and application of $SrRuO_3$ nanoparticles, while the average particle size of the synthesized products in our lab is smaller than those reported in the literature.[8b,14] It is found that the synergistic effect of $SrRuO_3$ nanoparticles and GQDs yields significant advantages in improving conductivity and catalytic activity and hence results in an impressive PCE of cells (8.05%), which is significantly higher than those of devices assembled with GQD based composite CEs.[4a,12,13]

2. Experimental section

2.1 Synthesis of $SrRuO_3$ nanoparticles and GQDs

Synthesis of $SrRuO_3$ nanoparticles. In this work, we developed a simple hydrothermal process to synthesize $SrRuO_3$ nanoparticles for the first time. A mixture of ruthenium(III) chloride hydrate ($RuCl_3 \cdot xH_2O$, 0.312 g), strontium chloride hydrate ($SrCl_2 \cdot xH_2O$, 0.620 g), sodium hydroxide (NaOH, 0.186 g) and oleic acid (3.503 g) were dissolved in 30 mL deionized water under vigorous stirring until fully dissolved. Afterwards, the mixture was transferred into a 100 mL Teflon-lined stainless autoclave, which was then heated to 200 °C and kept at this temperature for 48 h. After cooling, the final products were washed by repeated centrifugation with warm deionized water (60~80 °C), ethanol and cyclohexane sequentially. The resultant $SrRuO_3$ nanoparticles were collected after drying at 60 °C.

Synthesis of GQDs. A facile hydrothermal route was used for preparation of GQDs and a dialysis process was used to purify the as-prepared GQDs in this work. The detailed fabrication procedure of GQDs has been described in ref. 15. Typically, 0.841 g of citric acid and 0.913 g of thiourea were dissolved into 30 mL deionized water with magnetic stirring to obtain a clear solution, which was subsequently sealed in a 100 mL Teflon-lined stainless autoclave and kept in an oven at 180 °C for 12 h. After the autoclave was cooled naturally to room temperature, a transparent yellow solution was obtained. Then the solution was kept in a vacuum oven at 60 °C overnight to remove excess water. Subsequently, the mixture was dialyzed in a dialysis bag (material:

regenerated cellulose, retained molecular weight: 3500 daltons) for 8 hours to remove excess citric acid and/or thiourea. Then the water-soluble GQD dispersion retained in the dialysis bag was evaporated via vacuum drying. Next, the product was collected by adding ethanol into the homogeneous GQD suspension and then centrifugation at 8000 rpm for 20 min. Finally, 0.18 g freeze-dried GQDs was homogeneously redispersed in 30 mL deionized water and stored in the dark at room temperature.

2.2 Preparation of SRO–GQD CEs

0.178 g of the as-synthesized $SrRuO_3$ nanoparticles were added into a binder solution, which was prepared by mixing 7 mL of ethanol, 0.089 g of ethyl cellulose and 0.712 g terpinol under vigorous stirring for 20 min. Subsequently, the $SrRuO_3$ solution mixture was stirred with a magnetic bar for 2 h at room temperature and then dried via rotary evaporation at 45 °C to form the $SrRuO_3$ paste. Afterwards, the as-prepared $SrRuO_3$ paste was diluted with ethanol at a mass ratio of 2 : 7 and then cast onto the cleaned FTO glass substrates by spin coating at 2000 rpm for 30 s. The thickness of the $SrRuO_3$ mesoporous film can be controlled by changing the coating times. After annealing at 450 °C for 30 min, the residual solvent and binder can be removed, which greatly assists in strengthening the adhesion between the $SrRuO_3$ layer and the FTO substrate to afford the mesoporous $SrRuO_3$ CE. To investigate the influence of GQD decoration, a $SrRuO_3$ CE was dipped into the as-prepared GQD stock solution at room temperature for 8 h, 16 h, 24 h and 36 h. After vacuum drying at 60 °C overnight, $SrRuO_3$ CEs decorated with different loading amounts of GQDs can be prepared. For a good comparison, 50 μL of H_2PtCl_6 solution in ethanol was drop-cast onto the FTO glass substrate, followed by heat treatment at 400 °C for 30 min to obtain the conventional Pt CEs.

2.3 Assembly of DSSCs

Initially, FTO conductive glass substrates were sequentially washed with deionized water, ethanol, acetone, and isopropanol using an ultrasonic water bath for 20 min. TiO_2 precursor solution consisting of 0.04 M tetrabutyl titanate in isopropanol (containing 10 μL HCl per 5 mL of the above solution) was spin-cast onto the cleaned FTO substrates at 2000 rpm for 40 s, followed by sintering at 450 °C for 30 min in air, yielding a ~50 nm thick anatase TiO_2 compact layer. Subsequently, the commercial TiO_2 paste (Dyesol, 18NR-T) was diluted with ethanol in a weight ratio of 2 : 7, and then spread onto the as-prepared TiO_2 compact layer by a doctor blading method. When subjected to a calcination process at 150 °C for 15 min, 275 °C for 15 min, 350 °C for 10 min and finally 450 °C for 30 min in air sequentially, a ~12 μm thick TiO_2 mesoporous layer was formed. The resultant TiO_2 photoanode was immersed in 40 mM $TiCl_4$ solution for 60 min at 70 °C and then post-treated by annealing at 450 °C under air atmosphere for 60 min. After cooling down to 80 °C, the mesoporous TiO_2 photoanodes were immersed into a 0.5 mM ethanol solution of N719 dye ([cisdi(thiocyanato)-N,N'-bis(2,2'-bipyridyl-4-carboxylic acid)-4-tetrabutylammonium carboxylate]) (Solaronix Co., Ltd., Switzerland) for 20 h at room temperature. In the following

This journal is © The Royal Society of Chemistry 2017

J. Mater. Chem. A, 2017, **5**, 17848–17855 | **17849**

step, the dye sensitized TiO_2 photoanodes were scratched into a square with an active area of 0.16 cm² and then rinsed with ethanol to remove physically absorbed dye molecules. Finally, DSSC devices were constructed by sandwiching the redox electrolyte solution composed of 0.1 M LiI, 0.05 M I_2, and 0.5 M 4-*tert*-butylpyridine in 8 mL of acetonitrile between the as-prepared photoanodes and CEs. Similarly, the symmetrical dummy cell for electrochemical measurement was fabricated by sandwiching a redox electrolyte between two identical CEs.

2.4 Characterization techniques

The morphology and microstructure of the final products were observed on a field emission scanning electron microscope (FESEM, JSM-7600F, JEOL, Japan) equipped with an energy-dispersive X-ray spectrometer (EDS, NORAN System 7, Thermo Fisher, USA). Transmission electron microscopy (TEM, ARM200F, JEOL, Japan) images of GQDs and SRO–GQD CEs were obtained at an acceleration voltage of 200 kV. The crystal structures of $SrRuO_3$ nanoparticles were characterized using a powder X-ray Diffractometer (XRD, XRD-7000, SHIMADZU, Japan) with Cu K$_\alpha$ radiation ($\lambda = 1.54$ Å) operated at 40 kV and a current of 30 mA. Raman measurements were carried out on the as-synthesized GQDs using a Renishaw inVia Reflex microscope with an excitation wavelength of 532 nm. The four-point probe method was used to measure the electrical resistivity of $SrRuO_3$ and SRO–GQD samples, both of which were deposited on slide glass substrates. The cyclic voltammetry (CV) measurements were executed in a three electrode test system with different CEs as the working electrode, a Pt wire as the auxiliary electrode and Ag/AgCl electrode as the reference electrode at a scan rate of 50 mV s^{-1}. Three electrodes were dipped in an acetonitrile solution of 10 mM LiI, 1 mM I_2 and 0.1 M $LiClO_4$. Photocurrent density–voltage (*J*–*V*) characteristics of the assembled DSSCs were evaluated with a Keithley 2401 source meter under a solar simulator (Sun 3000 Solar Simulators, ABET Technologies, USA) with AM 1.5 G, 100 mW cm^{-2} illumination, which was calibrated by using a silicon reference solar cell.

Electrochemical impedance spectroscopy (EIS) measurements were performed on the symmetrical dummy cells (CE/electrolyte/CE) assembled with two identical CEs filled with the same electrolyte as that used in the DSSCs with an electrochemical workstation (CHI660c, CHI Instrument, Co. Ltd., China). The impedance studies were carried out by simulating open-circuit conditions with an AC modulation amplitude of 10 mV in a frequency range from 0.1 MHz to 100 mHz. The resultant Nyquist plots from EIS were analyzed using an equivalent circuit model by means of the Z-view software. Tafel polarization curves were determined by applying the same electrochemical workstation on the dummy cells with a scan rate of 10 mV s^{-1}.

3.   Results and discussions

A facile hydrothermal process is used to prepare $SrRuO_3$ nanoparticles for the first time. Fig. 1A presents the top view of the $SrRuO_3$ CE consisting of a great deal of $SrRuO_3$ nanoparticles with an average size of about 40 nm. The XRD pattern of $SrRuO_3$ nanoparticles is shown in Fig. 1B. The diffraction peaks at $2\theta = 32.23°$, $46.22°$ and $52.05°$ corresponding to the (121), (040) and (222) planes can be indexed to orthorhombic $SrRuO_3$ (JCPDF card no. 43-0472). GQDs were fabricated through a hydrothermal synthesis route and dialysis was chosen as the purification method for water soluble GQDs. A photographic image of the as-prepared GQD aqueous solution before dialysis treatment is shown in Fig. 1C, in which the well-dispersed GQD suspension appears pale yellow and is very stable. When the GQD suspension was subjected to dialysis in a dialysis bag (3500 Daltons) for 8 h and then freeze-drying treatment, the resultant GQDs with yellow aggregations can be obtained, as shown in Fig. 1D. Fig. S1† shows the absorption spectra of thiourea, citric acid and GQDs after hydrothermal treatment. It is obvious that there is an absorption peak at 331 nm no matter whether the GQDs are subject to dialysis treatment or not. The origin of this peak corresponds to $n \rightarrow \pi^*$ transition of the C=O bond.[15] However, the absorption peak at 222 nm for the GQDs before dialysis treatment is similar to
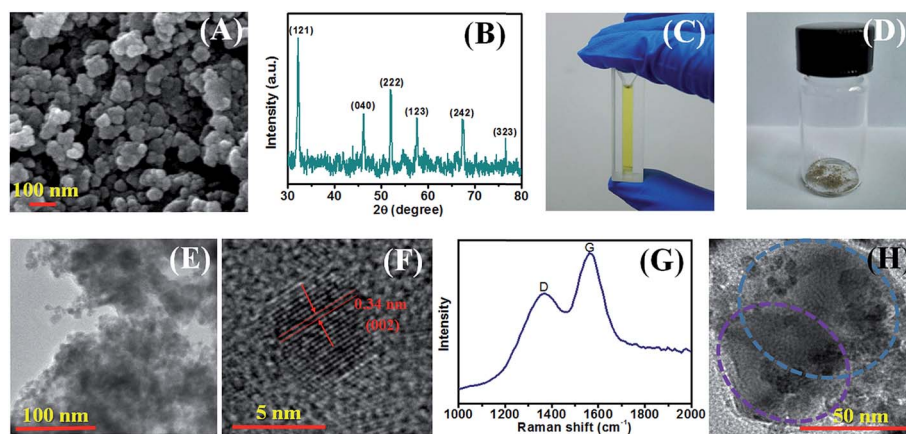

Fig. 1 (A) Top view FESEM image of a $SrRuO_3$ CE and (B) powder XRD pattern of the as-synthesized $SrRuO_3$ nanoparticles. Photograph of the (C) as-prepared GQD aqueous solution and (D) freeze-dried GQDs. (E) TEM image, (F) HRTEM image and (G) Raman spectrum of the synthesized GQDs. (H) TEM image of GQD decorated $SrRuO_3$ nanoparticles.

17850 | *J. Mater. Chem. A*, 2017, **5**, 17848–17855

This journal is © The Royal Society of Chemistry 2017

those of thiourea and citric acid, suggesting that the dialysis process can effectively purify the as-synthesized GQDs. The purified GQDs were dissolved in deionized water and stored in darkness at room temperature before use. As shown in Fig. 1E, the TEM image of the GQDs shows the presence of isolated GQDs with narrow size distribution in the range of 2–5 nm at the edge together with lots of aggregates, as a consequence of the strong tendency of GQDs to aggregate due to the face-to-face attraction between them.[16] A representative HRTEM image (Fig. 1F) displays a lattice spacing distance of 0.34 nm, which is ascribed to the graphite (002) facet. Fig. 1G shows Raman spectra with two characteristic peaks locating at 1375 cm^{-1} and 1572 cm^{-1}, which refer to the disordered (D) band and the crystalline (G) band, respectively.[17] The G band corresponds to the in-plane vibration of the symmetric sp^2 carbon oscillation of C–C bonds, which is related to E$_{2g}$ mode; while the D band is ascribed to the defect induced A$_{1g}$ mode, arising from lost carbon in the basal plane or from functionalities that disrupt the sp^2 bonding between carbon atoms in a perfect graphene crystal.[17] It is known that the ratio of the intensities (I_D/I_G) can be used to evaluate the quality of the as-prepared GQDs. I_D/I_G is equal to 0.74, indicating the highly crystalline and graphitic structure of GQDs. As shown in Fig. 1H, the TEM image of the SRO–GQD sample shows that GQDs are loaded on the surface of two partially overlapping SrRuO$_3$ nanoparticles, showing good contact between GQDs and SrRuO$_3$ nanoparticles. In addition, Fig. S2 and S3† present the TEM images containing multiple SrRuO$_3$ nanoparticles, and the corresponding EDS mappings (Fig. S3†) confirm that the elements Sr, Ru, and O are homogeneously distributed in the region where SrRuO$_3$ nanoparticles are located. It can be seen clearly that most of the surface of SrRuO$_3$ is decorated with uniform and dense GQDs.

Cyclic voltammetry (CV) measurements were carried out to evaluate the electrocatalytic activity of different CEs. As can be seen in Fig. 2, two pairs of redox peaks can be observed in each curve in the scanning range between +0.8 and −0.8 V. The right one with a more positive value corresponds to the redox reaction of I$_3^-$/I$_2$ (eqn (1)), while the left one corresponds to the redox reaction of I$^-$/I$_3^-$ (eqn (2)).[18] The photovoltaic performance of DSSCs is directly affected by the electrocatalytic activity towards the reduction of I$_3^-$ to I$^-$, which can be

evaluated by the current density of the reduction peak (J_{red}) and oxidation peak (J_{ox}) as well as the peak to peak splitting (E_{pp}).[4a]

$$2I_3^- \leftrightarrow 3I_2 + 2e^- \quad (1)$$

$$3I^- \leftrightarrow I_3^- + 2e^- \quad (2)$$

It is known that the rate constant of a redox reaction is inversely proportional to E_{pp}.[4l] Evidently, the conventional Pt film electrode has the smallest E_{pp} among the three CEs, suggesting the lowest overpotential for I$_3^-$ reduction[19] and the highest catalytic efficiency.[4l] However, the dramatically increased catalytic surface area of the mesoporous SrRuO$_3$ CE provides efficient transfer channels for electrolyte and electrons, giving rise to apparently increased J_{red} and J_{ox} compared to those of the Pt CE. Owing to the excellent intrinsic catalytic activity, the loaded GQDs ensure plenty of catalytically active sites. Besides, GQDs with good conductivity are responsible for connecting neighboring SrRuO$_3$ nanoparticles and facilitating the formation of a conductive network for the SRO–GQD CE, in accordance with the four-probe measuring results (4.5 × 10^{-2} Ω cm–5.9 × 10^{-2} Ω cm). Hence, the synergic effect of SrRuO$_3$ and GQDs provides multiple advantages in driving ion diffusion and collecting electrons from the external circuit as well as accelerating electron transfer to catalytic sites, thereby achieving high electrocatalytic capability towards the I$_3^-$/I$^-$ redox reaction. Such an improvement is also reflected in a smaller E_{pp} and higher J_{red} than those of SrRuO$_3$ CE. The schematic presentation of electron transportation and the electrocatalytic process responsible for catalyzing the reduction of I$_3^-$ to I$^-$ for SrRuO$_3$ and SRO–GQD CEs is visualized in Scheme 1.

The photovoltaic performances of DSSCs based on different CEs were evaluated by the current density–voltage (J–V) measurements under AM 1.5G one sun illumination, and the photovoltaic parameters are summarized in Table 1. PCE is defined as the cell's maximum power output density (P_{max}) divided by the input power density (100 mW cm^{-2}) from the standard light source and FF = $P_{max}/(J_{sc} \times V_{oc})$, where FF, J_{sc} and V_{oc} is the fill factor, short-circuit current density and open-circuit voltage of the cell, respectively. With increasing the thickness of coatings, the increased porosity and surface area allowed the diffusion of electrolyte easier and more I$_3^-$ involved

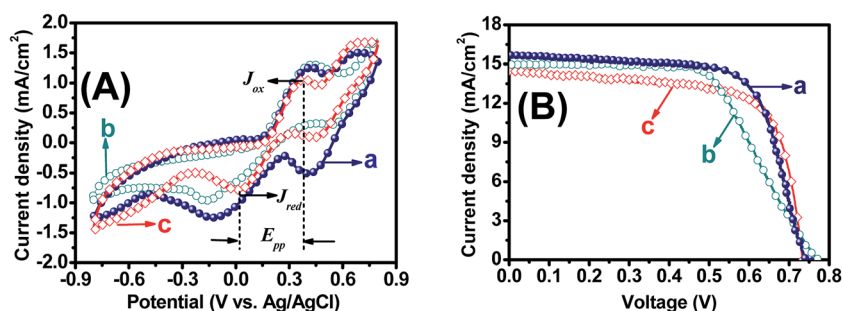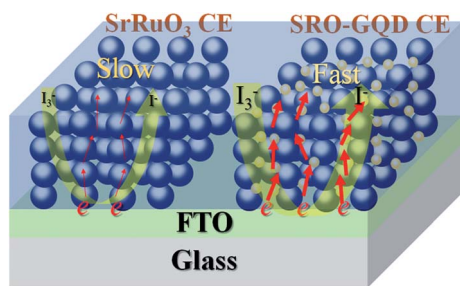**Fig. 2** (A) Cyclic voltammograms of different CEs recorded at a scan rate of 50 mV s^{-1} in an acetonitrile solution of 10 mM LiI, 1 mM I$_2$ and 0.1 M LiClO$_4$. (B) Photocurrent density–photovoltage (J–V) characteristics of the DSSCs using different CEs measured under AM 1.5 simulated solar illumination (100 mW cm^{-2}). (a) SRO–GQD CE, (b) SrRuO$_3$ CE and (c) Pt CE.

This journal is © The Royal Society of Chemistry 2017

J. Mater. Chem. A, 2017, **5**, 17848–17855 | **17851**

Scheme 1 The schematic diagram of the electrolyte regeneration reaction for $SrRuO_3$ and SRO–GQD hybrid CE.

Table 1 Photovoltaic parameters of DSSCs assembled with different CEs under one sun illumination (AM 1.5G, 100 mW cm^{-2})

| CEs	J_{sc} (mA cm^{-2})	V_{oc} (mV)	FF	PCE$_{max}$ (%)	PCE$_{ave}$[a] (%)
SrRuO$_3$	14.99	771	0.62	7.16	6.98 ± 0.18
SRO–GQD	15.62	758	0.68	8.05	7.97 ± 0.13
Pt	14.47	735	0.70	7.44	7.23 ± 0.16
SRO/MAO[9]	15.25	735	0.58	6.48	6.25

[a] The average values of PCE (PCE$_{ave}$) were obtained from five cells. The expansion of SRO/MAO is SrRuO$_3$/MgAl$_2$O$_4$, denoting the sputtered SrRuO$_3$ film deposited on a (100) oriented MgAl$_2$O$_4$ single crystal substrate.

in the redox reaction, while the reduced conductivity slowed down the electron collection from the external circuit. Consequently, the optimized DSSC based on a 1.14 μm-thick SrRuO$_3$ CE (Fig. S4†) exhibits a J_{sc} of 14.99 mA cm^{-2}, a V_{oc} of 771 mV and a FF of 0.62, resulting in a PCE of 7.16%, which outperforms the cell fabricated with the epitaxial sputtered SrRuO$_3$ film CE.[9] We have tried to use alternative techniques (such as spray coating, dip coating, and doctor blading) to deposit the mesoporous SrRuO$_3$ layer on the FTO substrate. However, these techniques resulted in a lower quality mesoporous layer due to obvious aggregation, non-uniform pore distribution and poor reproducibility of the films, compared with the spin coating technique. Furthermore, compared with the SrRuO$_3$ CE, the high electrocatalytic capability of the SRO–GQD hybrid one speeds up the reaction rate towards the reduction of I$_3^-$, which in turn boosts dye-regeneration and hence light capturing and

photoelectron injection, thereby resulting in an increased J_{sc}, in accordance with the IPCE results (Fig. S5†). In addition, the FF of the SRO–GQD device increases by 9.7% and an even higher percentage (17.2%) compared with the SrRuO$_3$ and SRO/MAO ones, respectively. The champion device based on the SRO–GQD CE exhibits an enhanced PCE of 8.05%, much higher than that of the reference Pt based device (7.44%).

A multi-cycle successive CV scan was conducted to investigate the long-term electrochemical stability of the SRO–GQD CE. Fig. 3A presents 30 consecutive cycle scans of the SRO–GQD CE at a scan rate of 50 mV s^{-1}, and the relationship between the cycle number and maximum redox peak current densities is also shown in Fig. 3B. Only a slight change between the first and 30th CV curves as well as the constant redox peak current densities can be observed, indicating an excellent long-term electrochemical stability of the SRO–GQD CE in the I$_3^-$/I$^-$ electrolyte system.

In order to provide insight into the charge transfer process and further evaluate the electrochemical activity of CE materials, EIS measurements are performed on the symmetrical dummy cells constructed with two identical SrRuO$_3$ or SRO–GQD electrodes so as to avoid the influence of the TiO$_2$ photoanode. Fig. 4A shows the Nyquist plots of the dummy cells, and the inset displays a typical equivalent circuit diagram used to analyze the Nyquist plots using the ZSimpWin software. Two semicircles are observed in the high-frequency (left) and low-frequency (right) region, respectively. The high-frequency intercept on the real axis represents the series resistance (R_s), mainly composed of the sheet resistance of the contact, electrodes, external wires, etc.[20] The left semicircle can be assigned to the charge-transfer impedance (R_{ct}) at the CE/electrolyte interface, and CPE represents the double layer capacitance. The right semicircle in the low frequency region can be assigned to the diffusion impedance of the redox couple in the electrolyte.[21] All the fitted EIS parameters extracted from the Nyquist plots are summarized in Table 2. It is found that the R_s value of the SRO–GQD CE (3.84 Ω cm^2) is smaller than that of the SrRuO$_3$ CE (5.19 Ω cm^2), which can be ascribed to the lower electrical resistivity of SRO–GQD than that of SrRuO$_3$. Moreover, SRO–GQD exhibits a lower R_{ct} (9.30 Ω cm^2) than SrRuO$_3$ (12.09 Ω cm^2), implying that the addition of GQDs speeds up the electron transfer processes that occur at the interface of the CE and
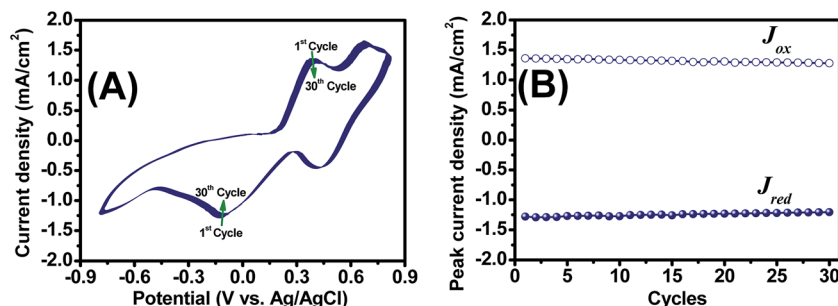
Fig. 3 (A) 30 continuous cycle CV scans and (B) the relationship between the cycles and the peak current density of the SRO–GQD CE with the scan rate of 50 mV s^{-1}.
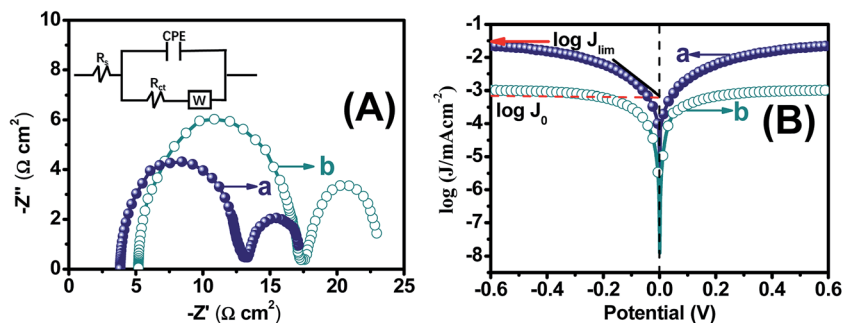
Fig. 4 (A) Nyquist plots derived from EIS of the symmetrical dummy cells. Equivalent circuit diagram used for the fitting of the Nyquist plots is inserted as the inset. (B) Tafel polarization curves of the symmetrical dummy cells. (a) SRO–GQD CE and (b) SrRuO$_3$ CE.

Table 2 The simulated EIS parameters of the dummy cell (CE/electrolyte/CE) fabricated with two identical SrRuO$_3$ or SRO–GQD electrodes

CE	R_s (Ω cm^2)	R_{ct} (Ω cm^2)	CPE (μF)
SrRuO$_3$	5.19	12.09	15.68
SRO–GQD	3.84	9.30	45.37

electrolyte. This is largely attributed to the formation of an effective pathway for electron transport provided by the sp^2 network, enabling a longer electron mean free path.[22] Such an enhancement results in the increased reduction rates of I$_3^-$/I$^-$ redox couples, in good agreement with the *C–V* results. In addition, lower R_s and R_{ct} of SRO–GQD also lead to a decreased total internal resistance, which is beneficial for the enhancement of the FF compared with SrRuO$_3$.[17,23] It is also noted that the CPEs of SRO–GQD and SrRuO$_3$ are 45.37 and 15.68 μF, respectively, which indicates that the SRO–GQD CE has a higher catalytic surface area than the SrRuO$_3$ CE, thereby contributing to the improvement of catalytic activity.[24]

To further characterize the catalytic abilities of SrRuO$_3$ and SRO–GQD CEs towards the I$_3^-$/I$^-$ redox reaction, Tafel polarization curves of dummy cells are presented in Fig. 4B. The exchange current density (J_0) and the limiting diffusion current density (J_{lim}) obtained from the Tafel curves are closely related to the catalytic activity of the CEs.[4h,25] J_0 is inversely proportional to R_{ct} according to eqn (3). Compared with SrRuO$_3$, SRO–GQD possesses a higher J_0 due to a larger slope for the anodic or cathodic branches, indicating a higher electrocatalytic activity

on the I$_3^-$/I$^-$ redox reaction, in good agreement with those trends derived from CV and EIS analyses. It is known that the diffusion coefficient (*D*) is proportional to the I$_3^-$ concentration gradient, which will increase the electrocatalytic ability of the CE towards the reduction of I$_3^-$ to I$^-$. Consequently, in addition to offering a larger J_0, the SRO–GQD CE also provides a larger J_{lim} than SrRuO$_3$, suggesting that SRO–GQD has a higher *D* according to eqn (4).

$$J_0 = \frac{RT}{nFR_{ct}} \tag{3}$$

$$D = \frac{l}{2nFC}J_{lim} \tag{4}$$

where *R* is the gas constant, *n* (*n* = 2) is the number of electrons involved in the reduction of I$_3^-$ at the electrode, *D* is the diffusion coefficient of the I$_3^-$, *l* is the spacer thickness, *T* is the thermodynamic temperature, *F* is the Faraday constant and *C* is the I$_3^-$ concentration in the redox electrolyte.

In the present work, SrRuO$_3$ CEs are soaked into GQD stock solution to obtain SRO–GQD CEs. To evaluate the influence of dipping time on the performance of cells and determine the optimal time, SrRuO$_3$ CEs are dipped into the as-prepared GQD stock solution for 8 h, 16 h, 24 h and 36 h at room temperature. The variation tendency of the photovoltaic parameters is shown in Fig. 5A and B. We can clearly see that the PCE initially increases with increased soaking time and then reaches a maximum efficiency of 8.05% at 24 hours, while a higher soaking time would lead to unsatisfactory results, especially a decrease in J_{sc} and FF. This is mainly due to the fact that
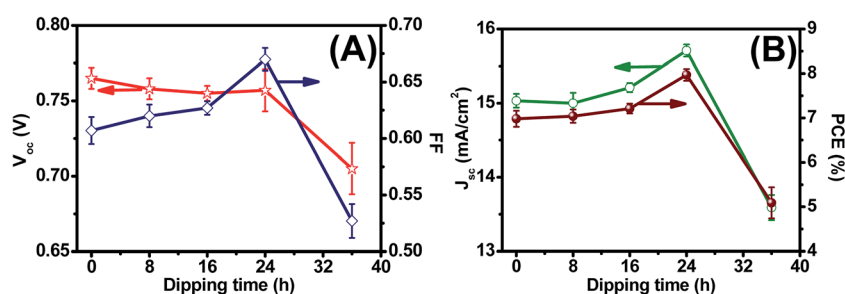

Fig. 5 Dipping time dependent (A) V_{oc} and FF and (B) J_{sc} and PCE of SRO–GQD CE based devices.

SrRuO$_3$ nanoparticles begin to fall off from the FTO substrate after being immersed for a long time, leading to the poor electron transfer process and the reduced number of active sites.

4. Conclusion

A mesoporous SrRuO$_3$ CE consisting of hydrothermally prepared SrRuO$_3$ nanoparticles with an optimized thickness demonstrates higher PCE (7.16%) than our published research on sputtered SRO film CEs (6.48%), which is largely due to the fact that the large interfacial contact area of the SrRuO$_3$ CE allows easier and faster diffusion of electrolyte into the pores and involves more I$_3^-$ in the redox reaction. Furthermore, the electrocatalytic activity toward I$_3^-$ reduction can be further improved for the device by applying a SRO–GQD hybrid CE, in which GQDs endowed with excellent intrinsic catalytic activity and high conductivity were incorporated into the SrRuO$_3$ CE matrix by a dipping technique. Such an enhancement benefits from more active catalytic sites provided by GQDs and the formation of a conductive network due to good connection between GQDs and SrRuO$_3$ nanoparticles. The predominant synergic effect of GQDs and SrRuO$_3$ CEs drives fast ion diffusion and collection of electrons from external circuits as well as electron transfer to catalytic sites. The champion device assembled with the optimized SRO–GQD CE yields an enhanced PCE of 8.05%, much higher than that of the reference cell fabricated with the Pt CE (7.44%). The SRO–GQD CE also shows an excellent long-term electrochemical stability in the I$_3^-$/I$^-$ electrolyte system. Hence, this work highlights the potential of employing SRO–GQD CEs as a promising candidate for use as Pt-free CEs in high-performance DSSCs.

Acknowledgements

References

1 (a) B. O'Regan and M. Grätzel, *Nature*, 1991, **353**, 737–740; (b) M. Grätzel, *Nature*, 2001, **414**, 338–344; (c) H. J. Snaith and L. Schmidt-Mende, *Adv. Mater.*, 2007, **19**, 3187–3200; (d) A. Yella, H. W. Lee, H. N. Tsao, C. Yi, A. K. Chandiran, M. K. Nazeeruddin, E. W. G. Diau, C. Y. Yeh, S. M. Zakeeruddin and M. Grätzel, *Science*, 2011, **334**, 629–634; (e) S. Mathew, A. Yella, P. Gao, R. H. Baker, B. F. E. Curchod, N. A. Astani, I. Tavernelli, U. Rothlisberger, M. K. Nazeeruddin and M. Grätzel, *Nat. Chem.*, 2014, **6**, 242–247; (f) Q. Jiang, Y.-P. Yeh, N. Lu, H. W. Kuo, M. Lesslie and T. Xu, *J. Renewable Sustainable Energy*, 2016, **8**, 013701.

2 (a) A. Hagfeldt, G. Boschloo, L. Sun, L. Kloo and H. Pettersson, *Chem. Rev.*, 2010, **110**, 6595–6663; (b) M. Wang, A. M. Anghel, B. Marsan, N.-L. C. Ha, N. Pootrakulchote, S. M. Zakeeruddin and M. Grätzel, *J. Am. Chem. Soc.*, 2009, **131**, 15976–15977.

3 J. H. Guo, Y. T. Shi, Y. T. Chu and T. L. Ma, *Chem. Commun.*, 2013, **49**, 10157–10159.

4 (a) C.-C. Wang and S.-Y. Lu, *Nanoscale*, 2015, **7**, 1209–1215; (b) H. Zhu, H. Zeng, V. Subramanian, C. Masarapu, K. H. Hung and B. Wei, *Nanotechnology*, 2008, **19**, 465204; (c) X. Xu, D. Huang, K. Cao, M. Wang, S. M. Zakeeruddin and M. Grätzel, *Sci. Rep.*, 2013, **3**, 1489; (d) R. Cruz, D. Alfredo, P. Tanaka and A. Mendes, *Sol. Energy*, 2012, **86**, 716–724; (e) J. Han, H. Kim, D. Y. Kim, S. M. Jo and S. Y. Jang, *ACS Nano*, 2010, **4**, 3503–3509; (f) P. Dong, C. L. Pint, M. Hainey, F. Mirr, Y. Zhan, J. Zhang, M. Pasquali, R. H. Hauge, R. Verduzco, M. Jiang, H. Lin and J. Lou, *ACS Appl. Mater. Interfaces*, 2011, **3**, 3157–3161; (g) C. T. Hsieh, B. H. Yang and J. Y. Lin, *Carbon*, 2011, **49**, 3092–3097; (h) H. Chen, T. Liu, J. Ren, H. He, Y. Cao, N. Wang and Z. Guo, *J. Mater. Chem. A*, 2016, **4**, 3238–3244; (i) H. Chen, T. Liu, N. Wang, L. Zhao, Q. Zhao, J. Ren, H. He and H. Lin, *Electrochim. Acta*, 2015, **174**, 871–874; (j) M. Wu, Y. N. Lin, H. Guo, W. Li, Y. Wang and X. Lin, *Nano Energy*, 2015, **11**, 540–549; (k) H. Wu, Z. Lv, Z. Chu, D. Wang, S. Hou and D. Zou, *J. Mater. Chem.*, 2011, **21**, 14815–14820; (l) J. D. Roy-Mayhew, D. J. Bozym, C. Punckt and I. A. Aksay, *ACS Nano*, 2010, **4**, 6203–6211.

5 (a) Q. Li, J. Wu, Q. Tang, Z. Lan, P. Li, J. Lin and L. Fan, *Electrochem. Commun.*, 2008, **10**, 1299–1302; (b) J. Kwon, V. Ganapathy, Y. H. Kim, K.-D. Song, H.-G. Park, Y. Jun, P. J. Yoo and J. H. Park, *Nanoscale*, 2013, **5**, 7838–7843.

6 (a) M. Wang, A. M. Anghel, B. t. Marsan, N.-L. Cevey Ha, N. Pootrakulchote, S. M. Zakeeruddin and M. Grätzel, *J. Am. Chem. Soc.*, 2009, **131**, 15976–15977; (b) M. Wu, L. Mu, Y. Wang, Y. Lin, H. Guo and T. Ma, *J. Mater. Chem. A*, 2013, **1**, 7519–7525; (c) X. Sun, J. Dou, F. Xie, Y. Li and M. Wei, *Chem. Commun.*, 2014, **50**, 9869–9871; (d) S. Shukla, N. H. Loc, P. P. Boix, T. M. Koh, R. R. Prabhakar, H. K. Mulmudi, J. Zhang, S. Chen, C. F. Ng, C. H. A. Huan, N. Mathews, T. Sritharan and Q. Xiong, *ACS Nano*, 2014, **8**, 10597–10605; (e) Y. C. Wang, D. Y. Wang, Y. T. Jiang, H. A. Chen, C. C. Chen, K. C. Ho, H. L. Chou and C. W. Chen, *Angew. Chem., Int. Ed.*, 2013, **52**, 6694–6698; (f) J. Xu, H. Xue, X. Yang, H. Wei, W. Li, Z. Li, W. Zhang and C. S. Lee, *Small*, 2014, **10**, 4754–4759; (g) B. He, X. Meng and Q. Tang, *ACS Appl. Mater. Interfaces*, 2014, **6**, 4812–4818; (h) Q. W. Jiang, G. R. Li and X. P. Gao, *Chem. Commun.*, 2009, **44**, 6720–6722; (i) Z. Yang, C.-Y. Chen, C.-W. Liu, C.-L. Li and H.-T. Chang, *Adv. Energy Mater.*, 2011, **1**, 259–264; (j) J. T. Park, C. S. Lee and J. H. Kim, *Nanoscale*, 2015, **7**, 670–678; (k) J. Wan, G. Fang, H. Yin, X. Liu, D. Liu, M. Zhao, W. Ke, H. Tao and Z. Tang, *Adv. Mater.*, 2014, **26**, 8101–8106; (l) Z. Sun, L. Zhang,

17854 | *J. Mater. Chem. A*, 2017, **5**, 17848–17855

This journal is © The Royal Society of Chemistry 2017

F. Dang, Y. Liu, Z. Fei, Q. Shao, H. Lin, J. Guo, L. Xiang, N. Yerra and Z. Guo, *CrystEngComm*, 2017, **19**, 3288–3298.

7 (*a*) K. Deshpande, A. Mukasyan and A. Varma, *J. Power Sources*, 2006, **158**, 60–68; (*b*) S. H. Chang, N. Danilovic, K. C. Chang, R. Subbaraman, A. P. Paulikas, D. D. Fong, M. J. Highland, P. M. Baldo, V. R. Stamenkovic, J. W. Freeland, J. A. Eastman and N. M. Markovic, *Nat. Commun.*, 2014, **5**, 4191.

8 (*a*) A. Lan and A. S. Mukasyan, *Ind. Eng. Chem. Res.*, 2008, **47**, 8989–8994; (*b*) N. F. Atta, A. Galal and S. M. Ali, *Int. J. Electrochem. Sci.*, 2012, **7**, 725–746.

9 T. Liu, J. Hou, B. Wang, F. Bai, H. Chen, L. Gao, Y. Cao, H. He, J. Wang, N. Wang, G. Cao and Z. Guo, *J. Mater. Chem. A*, 2016, **4**, 10794–10800.

10 K. S. Novoselov, A. K. Geim, S. V. Morozov, D. Jiang, Y. Zhang, S. V. Dubovos, I. V. Grigorieva and A. A. Firsov, *Science*, 2004, **306**, 666–669.

11 (*a*) L. Li, G. Wu, G. Yang, J. Peng, J. Zhao and J. J. Zhu, *Nanoscale*, 2013, **5**, 4015–4039; (*b*) L. Qian, Y. Zheng, J. Xue and P. H. Holloway, *Nat. Photonics*, 2011, **5**, 543–548; (*c*) N. Maity, A. Kuila, S. Das, D. Mandal, A. Shit and A. K. Nandi, *J. Mater. Chem. A*, 2015, **3**, 20736–20748; (*d*) X. Li, M. Rui, J. Song, Z. Shen and H. Zeng, *Adv. Funct. Mater.*, 2015, **25**, 4929–4947; (*e*) L. Zhang, W. Yu, C. Han, J. Guo, Q. Zhang, H. Xie, Q. Shao, Z. Sun and Z. Guo, *J. Electrochem. Soc.*, 2017, **164**, H651–H656; (*f*) K. Sun, P. Xie, Z. Wang, T. Su, Q. Shao, J. Ryu, X. Zhang, J. Guo, A. Shankar, J. Li, R. Fan, D. Cao and Z. Guo, *Polymer*, 2017, **125**, 50–57; (*g*) T. Wu, Q. Shao, S. Ge, *et al.*, *RSC Adv.*, 2016, **6**, 58020–58027; (*h*) S. Ge, X. Yang, Q. Shao, Q. Liu, T. Wang, L. Wang and X. Wang, *J. Solid State Chem.*, 2013, **200**, 136–142.

12 M. Dinari, M. M. Momeni and M. Goudarzirad, *J. Mater. Sci.*, 2016, **51**, 2964–2971.

13 L. Chen, C. X. Guo, Q. Zhang, Y. Lei, J. Xie, S. Ee, G. Guai, Q. Song and C. M. Li, *ACS Appl. Mater. Interfaces*, 2013, **5**, 2047–2052.

14 S. Pradhan, M. Sakil and G. S. Roy, *Researcher*, 2013, **5**(2), 44–46.

15 D. Qu, M. Zheng, P. Du, Y. Zhou, L. Zhang, D. Li, H. Tan, Z. Zhao, Z. Xie and Z. Sun, *Nanoscale*, 2013, **5**, 12272–12277.

16 M. Vázquez-Nakagawa, L. Rodríguez-Pérez, M. A. Herranz and N. Martín, *Chem. Commun.*, 2016, **52**, 665–668.

17 M. Giannouri, M. Bidikoudi, L. M. Pastrana-Martínez, A. M. T. Silvac and P. Falarasa, *Electrochim. Acta*, 2016, **219**, 258–266.

18 (*a*) V. D. Dao, L. L. Larina, K. D. Jung, J. K. Lee and H. S. Choi, *Nanoscale*, 2014, **6**, 477–482; (*b*) Q. H. Chang, L. Huang, J. Z. Wang, Z. J. Ma, P. P. Li, Y. Yan, J. X. Zhu, S. H. Xu, L. Shen, Q. Chen, Q. J. Yu and W. Z. Shi, *Carbon*, 2015, **85**, 185–193.

19 X. Cui, Z. Xie and Y. Wang, *Nanoscale*, 2016, **8**, 11984–11992.

20 Q. Wang, J.-E. Moser and M. Grätzel, *J. Phys. Chem. B*, 2005, **109**, 14945–14953.

21 (*a*) Z. B. Yang, M. K. Liu, C. Zhang, W. W. Tjiu, T. X. Liu and H. S. Peng, *Angew. Chem., Int. Ed.*, 2013, **52**, 3996–3999; (*b*) Y. H. Xue, J. Liu, H. Chen, R. G. Wang, D. Q. Li, J. Qu and L. M. Dai, *Angew. Chem., Int. Ed.*, 2012, **51**, 12124–12127; (*c*) H. Wang, K. Sun, F. Tao, D. J. Stacchiola and Y. H. Hu, *Angew. Chem., Int. Ed.*, 2013, **52**, 9210–9214.

22 (*a*) N. L. Yang, J. Zhai, D. Wang, Y. S. Chen and L. Jiang, *ACS Nano*, 2010, **4**, 887–894; (*b*) H. M. Ma, J. H. Tian, L. Cui, Y. Y. Liu, S. M. Bai, H. Chen and Z. Q. Shan, *J. Mater. Chem. A*, 2015, **3**, 8890–8895.

23 I. Han, N. Koide, Y. Chiba and T. Mitate, *Appl. Phys. Lett.*, 2004, **84**, 2433.

24 J. Jin, X. Zhang and T. He, *J. Phys. Chem. C*, 2014, **118**, 24877–24883.

25 E. Bi, Y. Su, H. Chen, X. Yang, M. Yin, F. Ye, Z. Li and L. Han, *RSC Adv.*, 2015, **5**, 9075–9078.